Reconstruction of two-dimensional velocity distribution in scramjet by laser absorption spectroscopy tomography

Reconstruction of 2D velocity distribution in scramjet by laser absorption spectroscopy tomography

QIANWEI QU,[1,2] ZHANG CAO,[1] LIJUN XU,[1,*] CHANG LIU,[3] LIUYONG CHANG,[1] HUGH MCCANN[3]

[1]Ministry of Education's Key Laboratory of Precision Opto-mechatronics Technology & School of Instrument Science and Opto-Electronic Engineering, Beihang University, Beijing 100083, China
[2]Shenyuan Honors College of Beihang University, Beijing 100083, China
[3]School of Engineering, The University of Edinburgh, Edinburgh EH9 3FB, Scotland UK
*Corresponding author: Lijun Xu (e-mail: lijunxu@buaa.edu.cn)

Received XX Month XXXX; revised XX Month, XXXX; accepted XX Month XXXX; posted XX Month XXXX (Doc. ID XXXXX); published XX Month XXXX

We propose a method to reconstruct the two-dimensional (2D) velocity distribution of flow fields by laser absorption spectroscopy tomography. A mathematic model is established to reveal the dependence of spectral absorbance on line-of-sight velocity distribution. Then, with multiple laser beams from different angular views covering the region of interest, a nonlinear equation set of 2D velocity distribution is established according to the model. The integrated absorbance coefficient distribution is reconstructed using the Landweber iteration algorithm and substituted into the nonlinear equation set for further simplification. Finally, the velocity distribution is reconstructed by solving the simplified equation group via the interior-point algorithm. The proposed method is validated numerically by reconstructing the velocity distribution of water molecules, as calculated by Computational Fluid Dynamics, over a cross-section of a double-mode scramjet combustor. The method does not require adding extra tracer particles and avoids issues arising from the short lifetime of molecular tags. It is suitable for diagnosis of high-speed flow fields.

OCIS codes: *(300.0300) Spectroscopy; (300.1030) Absorption; (110.6960) Tomography; (120.7250) Velocimetry.*

http://dx.doi.org/10.1364/AO.99.099999

1. INTRODUCTION

Velocity is a vital parameter in the investigation of aerodynamics [1] and combustion processes [2]. Velocimetry is therefore a topic that continues to draw the attention of many scientists in those areas [3–10].

Particle image velocimetry [7] (PIV) is one of the most commonly used methods to measure flow velocity distribution. In a PIV system, small tracer particles, added into the airflow, are illuminated by means of a thin light sheet. The displacements of the particles during a short time interval are recorded using two image frames. Then, the velocities of the particles are calculated based on cross correlation techniques and used to represent the velocity distribution of the airflow [11]. However, the added particles may lead to complications in PIV. For instance, the size of the tracer particles can be reduced by the high-power laser used in PIV systems. The time delay of the light sources should be long enough to capture the displacement of the tracer particles and short enough to ensure that those particles that have an out-of-plane velocity component remain within the light sheet. Another technique similar to PIV is molecular tagging velocimetry [8,12,13] (MTV). In MTV, the molecules in the airflow act as tracers, by being raised to an excited state from which their subsequent decay can be detected. The geometry of the region of interest (RoI) is defined by the high-power laser beams deployed in the excitation process. The RoI should be interrogated at two successive times within the excited-state lifetime of the selected tracer (OH, NO, excited O_2, etc.), which is a potential limitation of the technique. These molecules are always tagged by photo-dissociation, fluorescence, phosphorescence or other excitation techniques. The induced light may be extinct in some situations, e.g. fluorescence quenching.

It has been more than two decades since laser absorption spectroscopy (LAS) was first used to measure gas flow velocity [14–16]. The flow velocity is calculated according to the Doppler shift of the absorption spectrum of a target molecule. Additional tracers are unnecessary in LAS. Moreover, the lifetimes of the molecules are no more a barrier because LAS requires only absorption of the incident light and does not detect any light from de-excitation, i.e. LAS does not track individual molecules, and laser absorbance is determined by the statistical characteristic of all target molecules along the laser beam [17]. However, in previous applications, most efforts were devoted to line-of-sight LAS, which could only measure the bulk velocity of the gas flow. Gamba reported the reconstruction of the spatially-resolved velocity distribution [18]. In his work, the spectral absorbance profile was approximated by the discrete Fourier transform (DFT). Limited by the finite spectral ranges of devices, the absorbance profiles

are sometimes truncated, which can cause the DFT to become inaccurate. In the work reported here the problem was solved by modifying the model and reconstruction algorithm.

In this paper, we propose a LAS tomographic method to reconstruct 2D flow field velocity distributions. The mathematical model of our method is established in accordance with the Doppler spectral line shift of the target spectroscopic absorption. Combining with tomographic techniques, the velocity distribution is reconstructed by solving a nonlinear equation set directly. The method eliminates the adverse effects of isotropic line shifts and is not limited by truncation on the sampled absorbance. Reconstruction of a simulated velocity distribution validates the proposed method.

Laser absorption spectroscopy tomography has been used for the measurements of temperature, concentration and even pressure distributions for nearly two decades [19–27]. We show here that the velocity distribution can be synchronously reconstructed with all these parameters without any changes of the original measurement systems.

2. METHODOLOGY

A. Dependence of spectral absorbance on line-of-sight velocity distribution

According to the LAS theory [15,28], for a specified spectral line of a molecule, the absorbance ratio $\tau(\nu)$ at frequency ν is,

$$\ln\frac{I_0(\nu)}{I_t(\nu)}=\tau(\nu)=\int_0^L a(l)\varphi(\nu,l)\,\mathrm{d}l, \tag{1}$$

where, $I_0(\nu)$ and $I_t(\nu)$ are the incident and transmitted laser intensities, respectively; L is the optical length of the laser path; l is the local position where the laser interacts with the target molecule. The integrated absorbance coefficient $a(l)$ is expressed as [17],

$$a(l)=P(l)S(T(l)), \tag{2}$$

where $P(l)$ and $T(l)$ are the local partial pressure and local temperature, respectively; $S(T)$ is the temperature-dependent line strength function of the target transition [17].

The line shape function $\varphi(\nu,l)$ is approximated by the Voigt profile as [29–36],

$$\varphi(\nu-\Delta\nu(l);\sigma(l),\gamma(l))=\frac{1}{\pi\sqrt{2\pi}}\frac{\gamma(l)}{\sigma(l)}\int_{-\infty}^{+\infty}\frac{\exp\left(-t^2/\left(2\sigma^2(l)\right)\right)}{(\nu-\Delta\nu(l)-t)^2+\gamma^2(l)}\,\mathrm{d}t, \tag{3}$$

where $\sigma(l)$ and $\gamma(l)$ are Gauss and Lorentz broadening parameters, respectively. The spectral line is broadened due to different factors and two of those are modeled by the Voight profile: random thermal motions of molecules result in Doppler broadening, and the Gauss broadening parameter expresses this temperature dependence [17]; collisions between molecules result in so-called collisional broadening, and the Lorentz parameter expresses the effect of pressure and concentrations of various molecules [17]. The central frequency shift, $\Delta\nu(l)$, is the sum of two different parts, as

$$\Delta\nu(l)=\Delta\nu^{\mathrm{iso}}(l)+\Delta\nu^{\mathrm{D}}(l), \tag{4}$$

where $\Delta\nu^{\mathrm{iso}}(l)$ and $\Delta\nu^{\mathrm{D}}(l)$ are the isotropic shift and the anisotropic Doppler shift, respectively. The isotropic shift is the sum of the absorption line shifts that are not related to the directions of the laser beams, including the absolute central frequency of the spectral line, the pressure shift due to the interactions between two collision partners, the signal transmission delays, etc. The Doppler shift is caused by the local gas bulk velocity relative to the incident laser beam direction. As shown in Fig. 1, the flow velocity at l is $\boldsymbol{V}(l)$. The direction vector of the laser beam is $\boldsymbol{u}$, and the optical length in the gas is $\mathrm{d}l$. As a result, the Doppler shift of the absorption line is

$$\Delta\nu^{\mathrm{D}}(l)=\nu^{\mathrm{C}}\frac{\boldsymbol{V}(l)\cdot\boldsymbol{u}}{c}, \tag{5}$$

where ν^{C} is the original central frequency of the spectral line, and c is the speed of light.

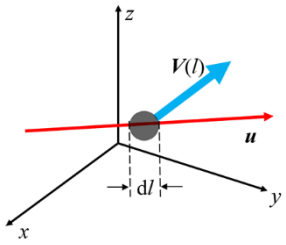

Fig. 1. Illustration of interaction between laser along direction $\boldsymbol{u}$ and local gas velocity $\boldsymbol{V}(l)$.

In Fig. 1, if the *z*-axis is perpendicular to the tomographic RoI, the direction vector of the laser beam is written as,

$$\boldsymbol{u}=(\cos\theta,\sin\theta,0), \tag{6}$$

where θ is the angle between $\boldsymbol{u}$ and *x*-axis.

Let

$$\boldsymbol{V}(l)=(V^x(l),V^y(l),V^z(l)), \tag{7}$$

then

$$\Delta\nu^{\mathrm{D}}(l)=\nu^{\mathrm{C}}\frac{V^x(l)\cos\theta+V^y(l)\sin\theta}{c}. \tag{8}$$

We rewrite $\Delta\nu^{\mathrm{D}}(l)$ as $\Delta\nu^{\mathrm{D}}(l,\theta)$ to indicate the representation more clearly. With Eqs. (1), (4) and (8), the relationship between the absorption spectrum and the velocity along the laser beam can be expressed as

$$\tau(\nu,\theta)=\int_0^L a(l)\times\varphi\left(\nu-\Delta\nu^{\mathrm{iso}}(l)-\nu^{\mathrm{C}}\frac{V^x(l)\cos\theta+V^y(l)\sin\theta}{c};\sigma(l),\gamma(l)\right)\mathrm{d}l. \tag{9}$$

Eq. (9) expresses the relationship between the line-of-sight velocity distribution and the spectral absorbance.

B. Discretization of the model

In a tomographic problem, a RoI is discretized into N cells. Partial pressure, temperature and velocity are assumed uniform in each cell. Then the integral equation (9) can be written as a summation equation,

$$\tau(\nu,\theta)=\sum_{n=1}^{N} l_n(\theta)a_n \times \varphi\left(\nu-\Delta\nu_n^{\mathrm{iso}}-\nu^{\mathrm{C}}\frac{V_n^x\cos\theta+V_n^y\sin\theta}{c};\sigma_n,\gamma_n\right), \tag{10}$$

where n is the index of the cell, $l_n(\theta)$ the optical length of the laser beam in the n-th cell. In addition, the number of laser beams is restricted to an integer, M. In Eq. (10), $\tau(\nu,\theta)$, $l_n(\theta)$ and θ are related to the position of laser beam. Thus, for the m-th laser beam,

$$\tau(\nu,\theta_m)=\sum_{n=1}^{N} l_n(\theta_m)a_n \times \varphi\left(\nu-\Delta\nu_n^{\mathrm{iso}}-\nu^{\mathrm{C}}\frac{V_n^x\cos\theta_m+V_n^y\sin\theta_m}{c};\sigma_n,\gamma_n\right). \tag{11}$$

As shown in Fig. 2, the absorbance profile is sampled at discrete frequency points, and the j-th frequency point is denoted ν_j . Then, we have a completely discrete equation,

$$\tau(\nu_j,\theta_m)=\sum_{n=1}^{N} l_n(\theta_m)a_n \times \varphi\left(\nu_j-\Delta\nu_n^{\mathrm{iso}}-\nu^{\mathrm{C}}\frac{V_n^x\cos\theta_m+V_n^y\sin\theta_m}{c};\sigma_n,\gamma_n\right). \tag{12}$$

The equation can be abbreviated to

$$\tau_{jm}=\sum_{n=1}^{N} l_{mn}a_n\varphi_{jmn}, \quad j=1,\ldots,J,\ m=1,\ldots,M. \tag{13}$$

where $\tau_{jm}=\tau(\nu_j,\theta_m)$ and

$$\varphi_{jmn}=\varphi\left(\nu_j-\Delta\nu_n^{\mathrm{iso}}-\nu^{\mathrm{C}}\frac{V_n^x\cos\theta_m+V_n^y\sin\theta_m}{c};\sigma_n,\gamma_n\right)$$

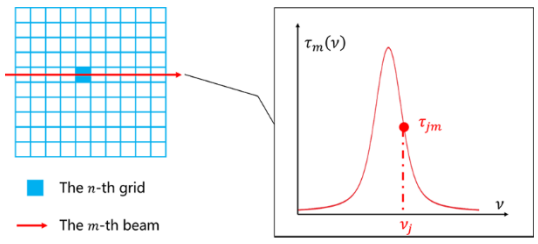

Fig. 2. Illustration of discrete LAS tomography. The region of interest (RoI) is divided into N cells with M laser beams penetrating the RoI. The absorbance profile of each beam is sampled at J frequency points.

C. Reconstruction of 2D velocity distribution

Following Eq. (13), a set of equations can be established with different j and m,

$$\begin{cases} \sum_{n=1}^{N} l_{1n}a_n\varphi_{11n} = \tau_{11}, \\ \vdots \\ \sum_{n=1}^{N} l_{mn}a_n\varphi_{jmn} = \tau_{jm}, \\ \vdots \\ \sum_{n=1}^{N} l_{Mn}a_n\varphi_{JMn} = \tau_{JM}. \end{cases} \tag{14}$$

The distribution of velocities in the RoI is reconstructed by solving the nonlinear system described by Eq. (14).

The line shape function is normalized, i.e.

$$\int_{-\infty}^{+\infty}\varphi(\nu,l)\,\mathrm{d}\nu=1. \tag{15}$$

Thus, for all frequency values, Eq. (1) can be rewritten as follows:

$$A=\int_{-\infty}^{+\infty}\tau(\nu)\,\mathrm{d}\nu=\int_0^L a(l)\,\mathrm{d}l, \tag{16}$$

where A is called the integrated absorbance. A discrete form of Eq. (16) is

$$A_m=\sum_{n=1}^{N} l_{mn}a_n. \tag{17}$$

The integrated absorbance coefficient distribution, $\{a_n \mid n=1,\ldots,N\}$ can be obtained by solving a linear equation group in advance [37,38],

$$\begin{cases} \sum_{n=1}^{N} l_{1n}a_n = A_1, \\ \vdots \\ \sum_{n=1}^{N} l_{mn}a_n = A_m, \\ \vdots \\ \sum_{n=1}^{N} l_{Mn}a_n = A_M. \end{cases} \tag{18}$$

The above equation can be rewritten as

$$\boldsymbol{La}=\boldsymbol{A}. \tag{19}$$

There are a number of methods to solve this linear inverse problem [39,40]. We adopt the Landweber iteration algorithm [24,37] in this work. The iteration starts from a uniform distribution and in the k-th step, the iteration point is updated by

$$\boldsymbol{a}^{(k+1)}=\boldsymbol{a}^{(k)}+\lambda^{(k)}\boldsymbol{L}^{\mathrm{T}}(\boldsymbol{A}-\boldsymbol{L}\boldsymbol{a}^{(k)}), \tag{20}$$

where $\lambda^{(k)}$ is the relaxation parameter. In each iteration, the relaxation parameter is selected using the line search algorithm [41].

Substituting the solution of Eq. (18) into Eq. (14), the 2D velocity distribution can be reconstructed by solving an equivalent nonlinear programming problem as

$$\min f = \sum_{j=1}^{J}\sum_{m=1}^{M}(\tau_{jm} - l_{mn}a_n\varphi_{jmn})^2.$$
$$\text{s.t. } c_1(\boldsymbol{x}) = 0, \quad c_2(\boldsymbol{x}) \le 0. \tag{21}$$

where $\boldsymbol{x}$ is the vector of all unknowns, and both $c_1(\boldsymbol{x})$ and $c_2(\boldsymbol{x})$ are constraint functions. Proper constraints can be given by *a priori* information.

The solution of Eq. (21) is the least square approximation of the solution of Eq. (14). In this paper, Eq. (21) is solved by using the interior point algorithm [42].

3. NUMERICAL STUDY AND DISCUSSIONS

A. Phantom Description

The method is validated numerically using the Computational Fluid Dynamics (CFD) simulation data of a double-mode scramjet combustor [43]. The main stream of the gas flow along the combustor is illustrated by the green arrow in Fig. 3(a). An inclined cross-section of the flow, marked in red in Fig. 3(a) is employed as the RoI. The distributions of velocity and integrated absorbance distribution are shown in Fig. 3 (b) and (c)

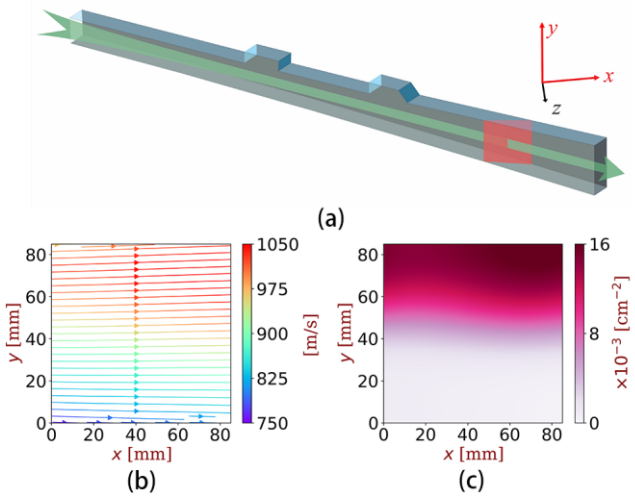

Fig. 3. Phantom for numerical experiment. (a) Object calculated by CFD. The green arrow illustrates the main steam direction in a double-mode scramjet combustor and the phantom is the cross-section marked in red. The other figures are the distribution of (b) velocity and(c) integrated absorbance coefficient distributions. The color map in (d) indicates the flow speed [m/s]

B. Numerical experiment

A H_2O transition near 1334 nm was selected. The spectral parameters of this line are obtained from HITRAN 2012 [44] and listed in Table 1, including its original central frequency ν^C, line strength function at 296 [K] $S(296)$, air-broadened half-width γ_{air}, self-broadened half-width γ_{self}, lower-state energy E'', temperature-dependence exponent n_{air}, and air pressure-induced line shift δ_{air}. This spectral line is isolated and has strong absorbance at high temperature. The absorbance profile (approximated by Puerta and Martin's algorithm [45]) of water vapor at 1500 [K], 0.4 [atm] is shown in Fig. 4.

Table 1. Spectral parameters of the selected spectral line

Parameters	Values	Units
ν^C	7495.504	cm^{-1}
$S(296)$	1.573×10^{-25}	cm^{-1} / (molecule cm^{-2})
γ_{air}	0.0524	cm^{-1} / atm
γ_{self}	0.195	cm^{-1} / atm
E''	4174.285	cm^{-1}
n_{air}	0.41	
δ_{air}	-0.00996	cm^{-1} / atm

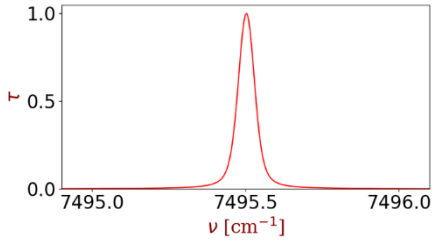

Fig. 4. The relative absorbance profile of H_2O from 7495 to 7496 [cm^{-1}] at 1500 [K] and 0.4 [atm]. The absorbance was calculated by using an online spectroscopic tool [46].

Forty-eight laser beams are launched into the region from four angular views, i.e., 0, 45, 90 and 135 degrees, and each beam has 200 sample points within the absorption feature. Thus, the total number of sample points is 9600. The beam arrangement is shown in Fig. 5.

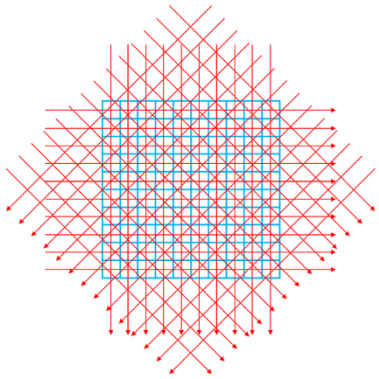

Fig. 5. Laser beam arrangement for numerical experiment.

In terms of the tomographic problem, the RoI is evenly divided into a 10×10 square grid; i.e. 100 cells. Random Gaussian noise is added independently to each simulated measurement of absorbance, and the standard deviation value of the noise is varied to yield measurement signal-to-noise ratio (SNR) values from 30 to 60 dB. The numerical simulations are repeated ten times in each noise condition. The values of SNR are calculated according to the total energy of absorbance signal and random noise. The energies of signal and noise are,

$$E^{\text{Signal}} = \sum_{m=1}^{M}\sum_{j=1}^{J}\tau_{mj}^2,$$
$$E^{\text{Noise}} = \sum_{m=1}^{M}\sum_{j=1}^{J}g_{mj}^2. \quad (22)$$

where g_{mj} is the value of Gaussian noises added to τ_{mj}. The value of SNR is calculated by

$$\text{SNR} = 10\lg\frac{E^{\text{Signal}}}{E^{\text{Noise}}}. \quad (23)$$

C. Results and analysis

The distribution of integrated absorbance coefficient was reconstructed firstly. The results corresponding to the SNR of 40 dB are shown in Fig. 6. As the values of some pixels are close to zero, the distribution of relative error in Fig. 6(b) is calculated as

$$e_n^{a\_\text{rel}} = \frac{a_n^{\text{recon}} - a_n^{\text{orig}}}{a^{\text{mean}}}, \quad (24)$$

where a_n^{recon} and a_n^{orig} are the reconstructed and original integrated absorbance coefficient, respectively. a^{mean} is the mean value of original integrated absorbance coefficient. The average relative error is 4.5 %.

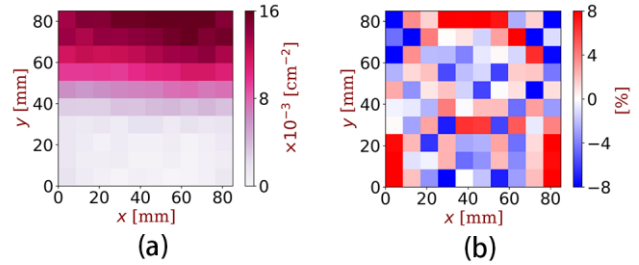

Fig. 6. Images of (a) reconstructed distribution of integrated absorbance coefficient when the SNR is 40 dB and (b) corresponding relative errors.

The values of integrated absorbance coefficient are substituted in Eq. (14), which is further solved by nonlinear programming to get the velocity distribution. The upper and lower bounds are given in the numerical case as constraints. The upper bound is 20% higher than the maximum value of the corresponding variables and the lower bound is 20 % lower than the minimum value of the corresponding variables.

The reconstructed results corresponding to 30, 40, 50 and 60 dB noise conditions are shown in Fig. 7. These results were calculated on a computer with an i7-4790 processor (3.6 GHz, without parallel acceleration). For 500 iterations of inner-point algorithm, we could get one reconstructed result in 12 minutes.

The streamlines of the images on the left column are calculated according to the mean value of reconstructed velocity distributions, i.e.

$$\left(V_n^x\right)^{\text{mean}} = \frac{1}{10}\sum_{k=1}^{10}\left(V_n^x\right)_k^{\text{recon}},$$
$$\left(V_n^y\right)^{\text{mean}} = \frac{1}{10}\sum_{k=1}^{10}\left(V_n^y\right)_k^{\text{recon}}. \quad (25)$$

The reconstructed velocity is located in the central of each pixel when the streamlines are calculated.

The streamlines of the images on the right column represent the distribution of relative errors. The color map corresponds to magnitude of relative error, i.e.

$$e_n^{V\_\text{m\_rel}} = \frac{\sqrt{\left[\left(V_n^x\right)^{\text{mean}} - \left(V_n^x\right)^{\text{orig}}\right]^2 + \left[\left(V_n^y\right)^{\text{mean}} - \left(V_n^y\right)^{\text{orig}}\right]^2}}{\sqrt{\left[\left(V_n^x\right)^{\text{orig}}\right]^2 + \left[\left(V_n^y\right)^{\text{orig}}\right]^2}}. \quad (26)$$

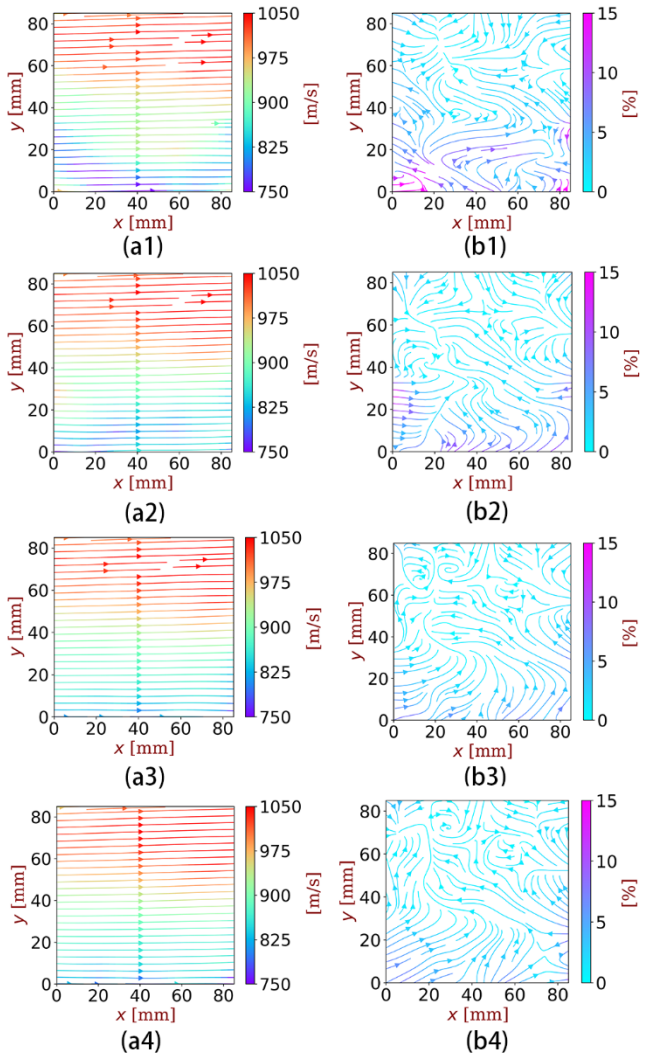

Fig. 7. Reconstructed velocity distributions. Streamlines in (a1) are calculated according to the mean values of reconstructed velocity distributions of ten simulations when the SNR is 30 dB. Streamlines in (b1) represent the relative reconstruction error corresponding to (a1). Similarly, (a2), (a3) and (a4) are the reconstructed results when the SNRs are 40, 50 and 60 dB, respectively. Their corresponding relative reconstruction errors are shown in (b2), (b3) and (b4), respectively.

As shown in Fig. 7, the velocity distribution is reconstructed with high fidelity. In other words, both the magnitudes and directions of the velocities fit those in the phantom. The reconstruction errors close to the lower boundary of the image are large, which is mainly caused by two factors. On one hand, the speeds in these pixels are slower than that of

others. On the other hand, the integrated absorbance coefficients in these pixels are smaller than that of others. The latter one makes the weights of the Doppler shifts of these pixels smaller than those of the others as indicated by Eq. (13). Meanwhile, the absorbance values corresponding to the laser beams through these pixels are smaller than those corresponding to the other beams. As a result, their profiles are more sensitive to random noise. In Fig. 8(b), two profiles of spectral absorbance corresponding to different laser beams are compared when the SNR is 40 dB: the original phantom (Figs. 3(b) and 3 (e)) shows that beam 2 traverses a region of much higher absorbance than is the case for beam 1, as reconstructed in Fig. 8(a); also, as determined by the original phantom (Fig. 3(d)), beam 2 traverses a region of significantly higher gas velocity than does beam 1. Fig. 8(b) shows that the spectral absorbance profile of τ_1 is obviously much more affected by noise than that of τ_2.

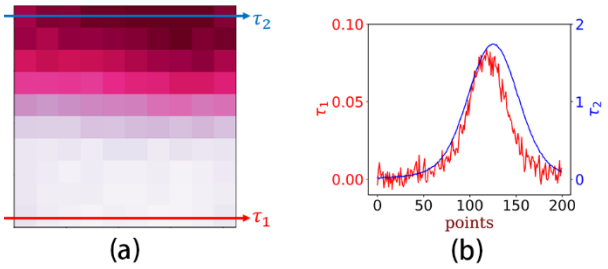

Fig. 8. Comparison of absorbance profiles along low and high absorbance laser beams. (a) reconstructed distribution of the integrated absorbance coefficient. (b) Absorbance profiles, τ_1 and τ_2, along the two laser beams shown in (a), when the SNR is 40 dB.

The quality of the reconstructed velocity distribution is evaluated by examining the root mean square error (RMSE) for each reconstructed distribution, i.e.

$$\mathrm{RMSE}_k = \frac{1}{N}\sum_{n=1}^{N}\sqrt{\frac{\left[\left(V_n^x\right)_k^{\mathrm{recon}}-\left(V_n^x\right)^{\mathrm{orig}}\right]^2+\left[\left(V_n^y\right)_k^{\mathrm{recon}}-\left(V_n^y\right)^{\mathrm{orig}}\right]^2}{\left[\left(V_n^x\right)^{\mathrm{orig}}\right]^2+\left[\left(V_n^y\right)^{\mathrm{orig}}\right]^2}}, \quad (27)$$

$k = 1, \ldots, 10.$

The mean values and standard deviations of RMSE as the SNR is varied from 30 to 60 dB are plotted in Fig. 9.

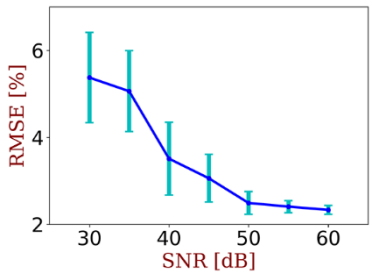

Fig. 9. Variation of RMSE with SNR.

Fig. 9 shows, for each SNR value, the mean RMSE of ten numerical simulations at that noise level, and the lengths of the error bars show the standard derivation in RMSE at that noise level. It can be seen that both the mean value and standard deviation of the RMSE decrease as the SNR increases, although the variation is very small for SNR above 50 dB.

D. Discussions

In Eq. (10), we use the sum formula to approximate the integration. Apparently, increasing the image resolution could improve the modeling accuracy, but makes Eq. (14) more complex in the meanwhile. Increasing one pixel means increasing five unknowns, i.e. σ_n, γ_n, $\Delta\nu_n^{\mathrm{iso}}$, V_n^x, and V_n^y, during the reconstruction of velocity distribution. This may dramatically affect the convergence property of the nonlinear programing iteration, making it slow and unstable.

The higher the flow speed along the laser beam, the greater the Doppler shift. Therefore, the method is suitable for reconstructing high-speed velocity distribution. The line shift is a part of line shape and small broadening parameters makes the spectral line more distinct with each other in different pixels. Thus, a 'thin' spectral line can improve the precision of resolving line shift. Thus, spectral line with smaller broadening coefficient is preferred in the proposed method. The line strength function should also be considered. In the above case, the selected spectral line is suitable for measurement at high temperature.

It is significant to point out that at least four laser beams from different projection views should pass through the voxels to decouple the two velocity components in a voxel. The line shift item in a voxel contains three unknowns, $\Delta\nu_n^{\mathrm{iso}}$, V_n^x, and V_n^y. To solve these unknowns, there should be at least three independent measurements.

Finally, we discuss the influence of the Fourier transform on the method. In the proposed work [18] the author used the Fourier transform to change the mathematical formulation of the reconstruction problem. In practice, the absorbance profile is sampled only a finite number of times in the sampling sequence and the continuous Fourier transform is approximated by the discrete Fourier transform (DFT). Conventionally, the original sequence is regarded as one cycle of a periodic signal. However, the absorbance profile is not periodic. The truncation of the profile may affect the accuracy of DFT as shown in Fig. 10. The sequence illustrated in Fig. 10 (a) is truncated and two subsequences are obtained as shown in Fig. 10 (b). Their DFTs (demonstrated in Fig. 10 (c) and (d)) are obvious different from each other and cannot be used to approximate the Fourier transform of original profile.

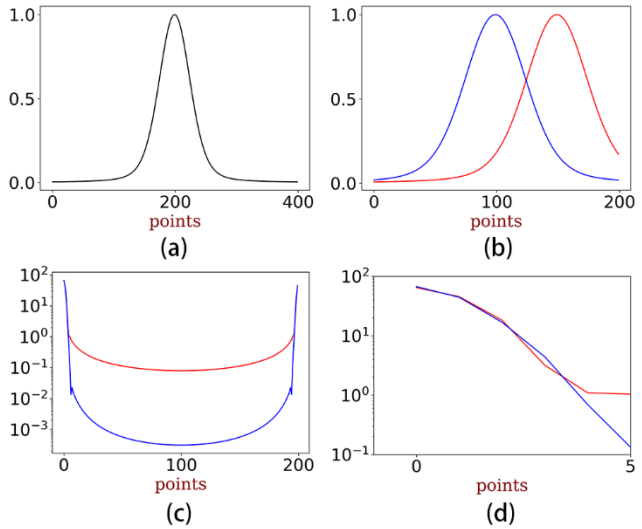

Fig. 10. Effects of truncation to the DFT of unimodal profile. (a) A sequence with 400 sample points. (b) Two subsequences of the original

sequence. (c) The amplitude of DFT of the subsequences. (d) Enlarged view of the low-frequency region of (c).

4. CONCLUSION

In this paper, we have presented a method for the reconstruction of 2D gas flow velocity distribution by laser absorption spectroscopy tomography.

The method was verified by a series of numerical simulations. The results indicate that the proposed method is valid in reconstructing the velocity distribution. The average value of image error, as expressed by RMSE, is less than 6% when the measurement SNR is greater than 30 dB, and it reduces with the increase of SNR. The integrated absorbance coefficient in a grid determines the weight of Doppler shift in this grid. Moreover, lower absorbance is more easily affected by random noise. Thus, the reconstruction error in the grid with higher absorbance is overall less than that in the grid with lower absorbance.

Funding Information. National Natural Science Foundation of China (No. 61620106004, No. 61522102, No. 61327011). Ministry of Science and Technology of the People's Republic of China (No. 2016YFF0100600). Hugh McCann and Chang Liu acknowledge funding support by the UK EPSRC via Platform Grant EP/P001661/1.

References

1. J. D. Anderson Jr., *Fundamentals of Aerodynamics* (Tata McGraw-Hill Education, 2010).
2. B. Lewis and G. Von Elbe, *Combusion, Flames and Explosions of Gases* (Elsevier, 2012).
3. S. A. Filatyev, J. F. Driscoll, C. D. Carter, and J. M. Donbar, "Measured properties of turbulent premixed flames for model assessment, including burning velocities, stretch rates, and surface densities," Combust. Flame **141**, 1–21 (2005).
4. X. R. Duan, W. Meier, P. Weigand, and B. Lehmann, "Phase-resolved laser Raman scattering and laser Doppler velocimetry applied to periodic instabilities in a gas turbine model combustor," Appl. Phys. B Lasers Opt. **80**, 389–396 (2005).
5. S. Dubsky, R. A. Jamison, S. C. Irvine, K. K. W. Siu, K. Hourigan, and A. Fouras, "Computed tomographic x-ray velocimetry," Appl. Phys. Lett. **96**, 023702 (2010).
6. M. S. Singh and H. Jiang, "Estimating both direction and magnitude of flow velocity using photoacoustic microscopy," Appl. Phys. Lett. **104**, 23–28 (2014).
7. M. Raffel, C. E. Willert, S. T. Wereley, and J. Kompenhans, *Particle Image Velocimetry* (Springer, 2007), Vol. 79.
8. R. W. Pitz, J. A. Wehrmeyer, L. A. Ribarov, D. A. Oguss, F. Batliwala, P. a DeBarber, S. Deusch, and P. E. Dimotakis, "Unseeded molecular flow tagging in cold and hot flows using ozone and hydroxyl tagging velocimetry," Meas. Sci. Technol. **11**, 1259–1271 (2000).
9. L. A. Ribarov, J. A. Wehrmeyer, R. W. Pitz, and R. A. Yetter, "Hydroxyl tagging velocimetry (HTV) in experimental air flows," Appl. Phys. B Lasers Opt. **74**, 175–183 (2002).
10. L. A. Ribarov, J. A. Wehrmeyer, S. Hu, and R. W. Pitz, "Multiline hydroxyl tagging velocimetry measurements in reacting and nonreacting experimental flows," Exp. Fluids **37**, 65–74 (2004).
11. C. Tropea, A. L. Yarin, and J. F. Foss, eds., *Springer Handbook of Experimental Fluid Mechanics* (Springer Science & Business Media, 2007).
12. R. W. Pitz, M. D. Lahr, Z. W. Douglas, J. A. Wehrmeyer, S. Hu, C. D. Carter, K.-Y. Hsu, C. Lum, and M. M. Koochesfahani, "Hydroxyl tagging velocimetry in a supersonic flow over a cavity," Appl. Opt. **44**, 6692–6700 (2005).
13. R. Pitz, "Hydroxyl Tagging Velocimetry," in *38th Fluid Dynamics Conference and Exhibit* (2008), pp. 1–18.
14. A. Y. Chang, M. D. Dirosa, D. F. Davidson, and R. K. Hanson, "Rapid tuning cw laser technique for measurements of gas velocity, temperature, pressure, density, and mass flux using NO," Appl. Opt. **30**, 3011–3022 (1991).
15. L. C. Philippe and R. K. Hanson, "Laser diode wavelength-modulation spectroscopy for simultaneous measurement of temperature, pressure, and velocity in shock-heated oxygen flows," Appl. Opt. **32**, 6090–6103 (1993).
16. L. S. Chang, C. L. Strand, J. B. Jeffries, R. K. Hanson, G. S. Diskin, R. L. Gaffney, and D. P. Capriotti, "Supersonic Mass-Flux Measurements via Tunable Diode Laser Absorption and Nonuniform Flow Modeling," Aiaa J. **49**, 2783–2791 (2011).
17. R. K. Hanson, R. M. Spearrin, and C. S. Goldenstein, *Spectroscopy and Optical Diagnostics for Gases* (Springer, 2016).
18. M. Gamba, "Multi-parameter estimation for spatially-resolved measurement of two-component velocity using absorption tomography," in *53rd AIAA Aerospace Sciences Meeting* (2015).
19. F. P. Hindle, S. J. Carey, K. Ozanyan, D. E. Winterbone, E. Clough, and H. McCann, "Measurement of gaseous hydrocarbon distribution by a near-infrared absorption tomography system," J. Electron. Imaging **10**, 593 (2001).
20. P. Wright, C. a Garcia-Stewart, S. J. Carey, F. P. Hindle, S. H. Pegrum, S. M. Colbourne, P. J. Turner, W. J. Hurr, T. J. Litt, S. C. Murray, S. D. Crossley, K. B. Ozanyan, and H. McCann, "Toward in-cylinder absorption tomography in a production engine," Appl. Opt. **44**, 6578–6592 (2005).
21. S. Pal, K. B. Ozanyan, and H. McCann, "A computational study of tomographic measurement of carbon monoxide at minor concentrations," Meas. Sci. Technol. **19**, 094018 (2008).
22. P. Wright, N. Terzija, J. L. Davidson, S. Garcia-Castillo, C. Garcia-Stewart, S. Pegrum, S. Colbourne, P. Turner, S. D. Crossley, T. Litt, S. Murray, K. B. Ozanyan, and H. McCann, "High-speed chemical species tomography in a multi-cylinder automotive engine," Chem. Eng. J. **158**, 2–10 (2010).
23. M. P. Wood and K. B. Ozanyan, "Simultaneous temperature, concentration, and pressure imaging of water vapor in a turbine engine," IEEE Sens. J. **15**, 545–551 (2015).
24. C. Liu, L. Xu, J. Chen, Z. Cao, Y. Lin, and W. Cai, "Development of a fan-beam TDLAS-based tomographic sensor for rapid imaging of temperature and gas concentration," Opt. Express **23**, 22494 (2015).
25. L. Xu, C. Liu, W. Jing, Z. Cao, X. Xue, and Y. Lin, "Tunable diode laser absorption spectroscopy-based tomography system for on-line monitoring of two-dimensional distributions of temperature and H2O mole fraction," Rev. Sci. Instrum. **87**, 013101 (2016).
26. W. Cai and C. F. Kaminski, "A tomographic technique for the simultaneous imaging of temperature, chemical species, and pressure in reactive flows using absorption spectroscopy with frequency-agile lasers," Appl. Phys. Lett. **104**, 034101 (2014).
27. W. Cai and C. F. Kaminski, "Multiplexed absorption tomography with calibration-free wavelength modulation spectroscopy," Appl. Phys. Lett. **104**, 154106 (2014).
28. M. P. Arroyo, S. Langlois, and R. K. Hanson, "Diode-laser absorption technique for simultaneous measurements of multiple gasdynamic parameters in high-speed flows containing water vapor," Appl. Opt. **33**, 3296–307 (1994).
29. E. E. Whiting, "An empirical approximation to the Voigt profile," J. Quant. Spectrosc. Radiat. Transf. **8**, 1379–1384 (1968).
30. J. J. Olivero and R. L. Longbothum, "Empirical Fits To Voigt Line-Width: a Brief Review," J. Quant. Spectrosc. Radiat. Transf. **17**, 233–236 (1977).
31. J. He and C. Zhang, "The accurate calculation of the Fourier transform of the pure Voigt function," J. Opt. A Pure Appl. Opt. **7**, 613–616 (2005).
32. J. Humlicek, "Optimized computation of the voigt and complex probability functions," J. Quant. Spectrosc. Radiat. Transf. **27**, 437–444 (1982).
33. J. Westberg, J. Wang, and O. Axner, "Fast and non-approximate methodology for calculation of wavelength-modulated Voigt lineshape functions suitable for real-time curve fitting," J. Quant. Spectrosc. Radiat. Transf. **113**, 2049–2057 (2012).
34. A. Berk, "Voigt equivalent widths and spectral-bin single-line transmittances: Exact expansions and the MODTRAN®5 implementation," J. Quant. Spectrosc. Radiat. Transf. **118**, 102–120 (2013).

35. N. H. Ngo, D. Lisak, H. Tran, and J. M. Hartmann, "An isolated line-shape model to go beyond the Voigt profile in spectroscopic databases and radiative transfer codes," J. Quant. Spectrosc. Radiat. Transf. **129**, 89–100 (2013).
36. L. Xu, C. Liu, D. Zheng, Z. Cao, and W. Cai, "Digital signal processor-based high-precision on-line Voigt lineshape fitting for direct absorption spectroscopy," Rev. Sci. Instrum. **85**, 0–9 (2014).
37. W. Q. Yang, D. M. Spink, T. A. York, and H. McCann, "An image-reconstruction algorithm based on Landweber's iteration method for electrical-capacitance tomography," Meas. Sci. Technol. **10**, 1065–1069 (1999).
38. C. Lindstrom, C.-J. Tam, R. Givens, D. Davis, and S. Williams, "Diode laser absorption tomography using data compression techniques," Comput. Imaging Vi **6814**, 1–17 (2008).
39. C. Liu and L. Xu, "Laser absorption spectroscopy for combustion diagnosis in reactive flows: A review," Appl. Spectrosc. Rev. **4928**, 1–44 (2018).
40. W. Cai and C. F. Kaminski, "Tomographic absorption spectroscopy for the study of gas dynamics and reactive flows," Prog. Energy Combust. Sci. **59**, 1–42 (2017).
41. P. C. Hansen and M. Saxild-Hansen, "AIR tools - A MATLAB package of algebraic iterative reconstruction methods," J. Comput. Appl. Math. **236**, 2167–2178 (2012).
42. R. H. Byrd, M. E. Hribar, and J. Nocedal, "An Interior Point Algorithm for Large-Scale Nonlinear Programming," SIAM J. Optim. **9**, 877–900 (1998).
43. Z. Yan, L. Yuzhen, L. Wei, W. Jianchen, and X. Xu, "Numerical Simulation of a Dual-Mode Scramjet Combustor," in *50th AIAA/ASME/SAE/ASEE Joint Propulsion Conference* (AIAA, 2014).
44. L. S. Rothman, I. E. Gordon, Y. Babikov, A. Barbe, D. Chris Benner, P. F. Bernath, M. Birk, L. Bizzocchi, V. Boudon, L. R. Brown, A. Campargue, K. Chance, E. A. Cohen, L. H. Coudert, V. M. Devi, B. J. Drouin, A. Fayt, J. M. Flaud, R. R. Gamache, J. J. Harrison, J. M. Hartmann, C. Hill, J. T. Hodges, D. Jacquemart, A. Jolly, J. Lamouroux, R. J. Le Roy, G. Li, D. A. Long, O. M. Lyulin, C. J. Mackie, S. T. Massie, S. Mikhailenko, H. S. P. Müller, O. V. Naumenko, A. V. Nikitin, J. Orphal, V. Perevalov, A. Perrin, E. R. Polovtseva, C. Richard, M. A. H. Smith, E. Starikova, K. Sung, S. Tashkun, J. Tennyson, G. C. Toon, V. G. Tyuterev, and G. Wagner, "The HITRAN2012 molecular spectroscopic database," J. Quant. Spectrosc. Radiat. Transf. **130**, 4–50 (2013).
45. J. Puerta and P. Martin, "Three and four generalized Lorentzian approximations for the Voigt line shape," Appl. Opt. **20**, 3923 (1981).
46. C. S. Goldenstein, V. A. Miller, R. Mitchell Spearrin, and C. L. Strand, "SpectraPlot.com: Integrated spectroscopic modeling of atomic and molecular gases," J. Quant. Spectrosc. Radiat. Transf. **200**, 249–257 (2017).